OPEN ACCESS



Global Compressive Oscillations in the Outer Solar Corona Driven by an Extreme Coronal Mass Ejection

Suzana S. A. Silva¹, J. J. González-Avilés², Pete Riley³, Michal Ben-Nun³, Erico L. Rempel⁴, Leonardo F. G. Batista⁵, Gary Verth⁶, Istvan Ballai⁶, Chia-Hsien Lin⁷, Luiz A. C. A. Schiavo⁸, and Viktor Fedun¹, Plasma Dynamics Group, School of Electrical and Electronic Engineering, University of Sheffield, Sheffield S1 3JD, UK; suzana.silva@sheffield.ac.uk² Escuela Nacional de Estudios Superiores (ENES) Unidad Morelia, Universidad Nacional Autónoma de México, 58190 Morelia, Michoacán, Mexico

3 Predictive Science Inc., 9990 Mesa Rim Rd., Ste. 170, San Diego, CA 92121, USA

4 Department of Mathematics, Aeronautics Institute of Technology, Praça Marechal Eduardo Gomes 50, 12228-900, São José dos Campos, SP, Brazil

Departamento de Física, Universidade Federal do Ceará, 6030 Campus do Pici, 60455-900, Fortaleza, CE, Brazil
 Plasma Dynamics Group, School of Mathematical and Physical Sciences, University of Sheffield, Sheffield S3 7RH, UK
 Department of Space Science and Engineering, National Central University, Taoyuan, Taiwan
 Department of Mathematics, Physics and Electrical Engineering, Northumbria University, Newcastle NE1 8ST, UK
 Received 2025 July 21; revised 2025 October 14; accepted 2025 November 1; published 2025 November 18

Abstract

Coronal mass ejections are known drivers of large-scale waves in the low corona. However, wave dynamics in the extended corona and inner heliosphere remain largely unexplored. Here, we report the first observational and numerical evidence of coherent global compressive oscillations in the outer corona and inner heliosphere, revealed by white-light Solar and Heliospheric Observatory Large Angle and Spectrometric Coronagraph (LASCO) C3 data and an MHD simulation. Analyzing the coronal mass ejection event of 2012 July 23 using spectral proper orthogonal decomposition, we isolate two distinct wave signatures: (1) a directional fast-mode shock-like compressive wave that dissipates completely within 3 hr, and (2) a large-scale global circular wave front consistent with fast-mode MHD behavior, lasting 7 hr and extending across the LASCO C3 field of view, marking the first detection of such a global oscillation. Our findings reveal a previously unrecognized component of coronal mass ejection—driven wave activity, providing new constraints on the dynamics of the extended corona and inner heliosphere.

Unified Astronomy Thesaurus concepts: Solar coronal mass ejections (310); Solar coronal waves (1995); Heliosphere (711)

1. Introduction

Coronal mass ejections (CMEs) are some of the most violent and energetic phenomena in the solar atmosphere, driving massive amounts of magnetized plasma into the heliosphere. Expanding into the corona, CMEs drive the solar wind through a magnetic field environment and are instrumental in the generation of various magnetohydrodynamic (MHD) wave modes. These waves provide valuable information on the dynamics of CMEs and are important in influencing space weather (P. F. Chen et al. 2005; Y. Chen 2013).

A key manifestation of CME activity in the low corona is the appearance of expanding, annular extreme-ultraviolet (EUV) waves, first detected by the Extreme Ultraviolet Imaging Telescope (EIT) instrument and now observed in unprecedented detail. These so-called "EIT" or EUV waves typically propagate at speeds of 200–400 km s⁻¹ but can reach or exceed 1000 km s⁻¹ in extreme cases; see, e.g., I. Ballai et al. (2005), B. J. Thompson & D. C. Myers (2009), and A. Warmuth (2011). Although early studies strongly linked EUV waves to CMEs and only weakly linked them to solar flares (D. A. Biesecker et al. 2002), their physical nature remains debated. Some researchers interpret EUV waves as true fast-mode MHD waves, while others observe them as pseudowaves, large-scale signatures of coronal restructuring

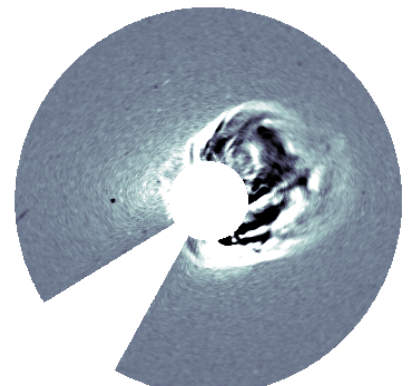
Original content from this work may be used under the terms of the Creative Commons Attribution 4.0 licence. Any further distribution of this work must maintain attribution to the author(s) and the title of the work, journal citation and DOI.

driven by the expanding CME (M. Wills-Davey et al. 2007; H. Wang et al. 2009). Also, R.-Y. Kwon et al. (2013) and R.-Y. Kwon et al. (2014) support a hybrid view, in which EUV waves often embody both a fast-mode wave front and a nonwave component associated with coronal magnetic reconfiguration.

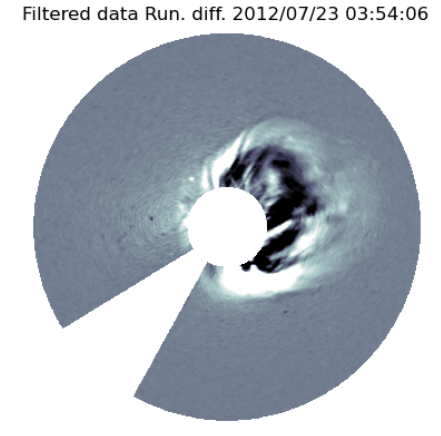
Fast CMEs are also well known for generating shocks, typically observed as type II radio bursts, and propagating at velocities of 500–2000 km s⁻¹, or higher in extreme events (N. Gopalswamy et al. 2008). The formation mechanisms for these shocks can vary, with piston-driven shocks occurring during the early impulsive CME phase and bow shocks forming ahead of the CME front as it propagates outward (B. Vršnak & E. W. Cliver 2008; A. M. Veronig et al. 2010; R.-Y. Kwon et al. 2014).

Recent observations and simulations have further revealed that CME eruptions can excite propagating shocks and large-scale coherent coronal oscillations. For instance, A. M. Veronig et al. (2010), Y. D. Liu et al. (2017), and N. Gopalswamy et al. (2016) demonstrate that CME-driven shocks and their global imprints can envelop the entire solar disk, sometimes persisting for hours, and cover the full solar corona, including polar coronal holes (W. Liu et al. 2018). Such global responses can include compressive standing modes and oscillations, suggesting a more intricate dynamical coupling between CME-driven disturbances and the extended corona than previously appreciated.

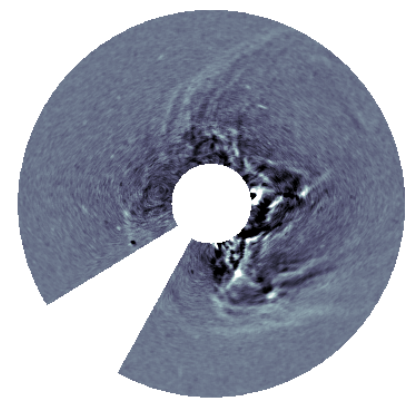
In this Letter, we present the first combined observational and numerical evidence for the simultaneous excitation of a fast-mode compressive front consistent with a shock in the outer corona and a global circular wave front in the outer Original data Run. diff. 2012/07/23 03:54:06



Original data Run. diff. 2012/07/23 05:54:06



Filtered data Run. diff. 2012/07/23 05:54:06



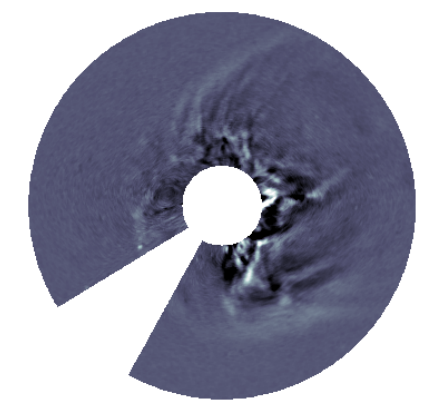


Figure 1. Running-difference LASCO C3 images of the 2012 July 23 CME at two representative times (03:54:06 UT, top row; 05:54:06 UT, bottom row). Left: original data. Right: filtered data after applying a Savitzky–Golay filter along the radial direction (window length 5, polynomial order 2) and a 10×10 median filter in the image plane.

corona and inner heliosphere, triggered by the extreme CME of 2012 July 23, a benchmark event for large-scale wave generation in the solar corona (D. N. Baker et al. 2013; C. T. Russell et al. 2013). We isolated and characterized the dual-wave response to the CME using spectral proper orthogonal decomposition (SPOD) analysis of Solar and Heliospheric Observatory (SOHO) Large Angle and Spectrometric Coronagraph (LASCO) C3 data and a 3D MHD simulation. Our findings highlight how the CME excites multiple MHD wave components, including localized compressive fronts and global coronal oscillations, as revealed through modal decomposition.

2. Data and Methods

2.1. The 2012 July 23 CME Event

The 2012 July 23 CME event originated from active region 11,520 on the far side of the Sun near S17W141 (heliographic longitude $\sim\!141^\circ$), producing a moderate solar energetic particle event. The eruption was directed away from Earth toward 125° W. N. Gopalswamy et al. (2014) estimated the CME's leading-edge speed to be $\sim\!2600~{\rm km~s^{-1}}$ using the graduated cylindrical shell model applied to combined SOHO and STEREO data. The first column of Figure 1 shows the running difference of original LASCO C3 images of the 2012 July 23 CME at two representative times (03:54:06 UT, top row; 05:54:06 UT, bottom row). To suppress the noise and strengthen faint coronal structures, we first applied a median

filter (T. Huang et al. 1979) with a window size of 10×10 pixels to remove isolated noise and to keep physical structures such as high gradients or propagating wave fronts. Following this step, the temporal sequence of the images was smoothed in the time domain with a Savitzky–Golay filter (A. Savitzky & M. J. E. Golay 1964; five frame window) to filter out high-frequency temporal noise without sacrificing essential features in the original LASCO C3 data. This preprocessing was necessary to perform a reliable study and avoid noise-related artifacts in the subsequent results. The running differences of the filtered data are displayed in the second column of Figure 1, showing that the filtering enhances large-scale CME structures while suppressing pixel-scale noise and background fluctuations.

2.2. Spectral Proper Orthogonal Decomposition

To identify coherent wave structures, we applied the SPOD, an extension of the classical proper orthogonal decomposition (POD) that extracts dominant spatial modes from time-dependent data. Given a field variable $q(\mathbf{x}, t)$, we define its fluctuation as

$$q'(\mathbf{x}, t) = q(\mathbf{x}, t) - \langle q(\mathbf{x}) \rangle, \tag{1}$$

where $\langle \cdot \rangle$ denotes the temporal mean, t is time, and x is the position vector. The decomposition is given by

$$q'(\mathbf{x}, t) = \sum_{n=1}^{N} \phi^{(n)}(\mathbf{x}) a^{(n)}(t),$$
 (2)

where N is the number of snapshots used in the decomposition, $\phi^{(n)}(x)$ is the spatial mode and $a^{(n)}(t)$ the temporal mode, and n superscript means the mode number. The modal basis is obtained by solving the eigenvalue problem $C\xi = \Lambda \xi$, where C is a covariance matrix, ξ is the eigenvector matrix, and Λ is a diagonal eigenvalue matrix. The temporal covariance matrix elements for datacube images is defined as

$$C_{t_1,t_2} = \frac{1}{N} \int_{\Omega} q'(\mathbf{x}, t_1) q'(\mathbf{x}, t_2) d\mathbf{x}, \tag{3}$$

where t_1 and t_2 are time frame numbers. For the analysis of 3D MHD simulations, vectorial SPOD is more suitable, as it captures the joint dynamics of all vector field components. In this case, Equation (3) becomes

$$C_{t_1,t_2} = \frac{1}{N} \int_{\Omega} v'(x, t_1) \cdot v'(x, t_2) dx, \tag{4}$$

where \mathbf{v}' is the velocity vector fluctuations defined in the same way as in Equation (1). SPOD differs from traditional POD by applying a filter to the covariance matrix as discussed by M. Sieber et al. (2016). The spatial modes are obtained as

$$\phi^{(n)}(\mathbf{x}) = \frac{1}{\lambda_n N} \sum_{i=1}^N \xi_{j,n} \ q'(\mathbf{x}, t_j), \tag{5}$$

where λ_n is the eigenvalue n of the eigenvalue matrix Λ . The temporal amplitude of each mode is given by

$$a^{(n)}(t_j) = \sqrt{N\lambda_n} \,\, \boldsymbol{\xi}_{j,n}. \tag{6}$$

The temporal amplitude $a^{(n)}(t)$ describes the time evolution of the *n*th mode, enabling identification of coherent wave dynamics and their temporal characteristics such as frequency, growth, or decay.

2.3. Numerical Model

To simulate CME propagation through a steady-state solar wind, we used sunRunner3D, a 3D MHD model that extends the earlier 1D version, SunRunner1D (P. Riley & M. Ben-Nun 2022). SunRunner3D has been previously applied to model CME structures (P. Riley et al. 2025), interpret the global heliospheric structure from in situ data using simulations (J. J. González-Avilés et al. 2024), assess numerical effects in solar wind simulations (L. De León-Alanis et al. 2024), and reproduce stream/corotating interaction regions observed by Parker Solar Probe and STEREO-A (E. Aguilar-Rodriguez et al. 2024).

Here, sunRunner3D employs boundary conditions from CORona-HELiosphere (CORHEL; J. A. Linker et al. 2009) and solves the ideal MHD equations using the PLUTO code (A. Mignone et al. 2007). The conservative form of the equations is

$$\frac{\partial \varrho}{\partial t} + \nabla \cdot (\varrho \mathbf{v}) = 0, \tag{7}$$

$$\frac{\partial(\varrho \mathbf{v})}{\partial t} + \nabla \cdot (\varrho \mathbf{v} \mathbf{v} - \mathbf{B} \mathbf{B} + p_t \mathbf{I}) = \varrho \mathbf{g}, \tag{8}$$

$$\frac{\partial E}{\partial t} + \nabla \cdot ((E + p_t)\mathbf{v} - \mathbf{B}(\mathbf{v} \cdot \mathbf{B})) = \varrho \mathbf{v} \cdot \mathbf{g}, \tag{9}$$

$$\frac{\partial \mathbf{B}}{\partial t} + \nabla \cdot (\mathbf{v}\mathbf{B} - \mathbf{B}\mathbf{v}) = 0, \tag{10}$$

$$\nabla \cdot \mathbf{B} = 0, \tag{11}$$

where ϱ is the mass density, \boldsymbol{B} the magnetic field, $p_t = p + B^2/2$ the total pressure, and \boldsymbol{I} the identity matrix. The total energy is $E = p/(\gamma - 1) + \varrho v^2/2 + B^2/2$, with $\gamma = 5/3$, $p = \varrho k_B T/\bar{m}$. Here, T is the temperature of the plasma, $\bar{m} = \mu m_p$ is the particle mass specified by a mean molecular weight value $\mu = 0.6$ for a fully ionized gas, m_p is the proton mass, and k_B is the Boltzmann constant. Gravity is modeled as $\boldsymbol{g} = -GM_{\odot}/r^2\,\hat{\boldsymbol{r}}$, with G representing the gravitational constant, M_{\odot} the solar mass, and r the radial direction. In this Letter, we show the results in terms of the proton number density N_p and proton temperature T_p , instead of the mass density ρ and plasma temperature T_p , instead of the mass density of and plasma in which protons dominate both mass and thermal properties.

Equations (7)–(11) are solved in 3D spherical coordinates (r, θ, ϕ) , including solar rotation in longitude (ϕ) at a rate equal to $\Omega_c = 2.8653 \times 10^{-6}$ Hz (J. Pomoell & S. Poedts 2018; P. Mayank et al. 2022). The domain spans 0.14–1.1 au in $r, \theta \in [0, \pi]$ and $\phi \in [0, 2\pi]$, with resolution 141 × 111 × 128. We use Runge-Kutta (RK2) time-stepping, second-order reconstruction with minmod limiter, the Harten, Lax and van Leer (HLL) Riemann solver (A. Harten et al. 1997), and Powell's eight-wave method (K. G. Powell 1997) for magnetic divergence control. Boundary conditions include CORHEL input at 0.14 au, outflow at 1.1 au, polar axis treatment with the ring-average method in θ (B. Zhang et al. 2019), and periodicity in ϕ .

2.3.1. CME Model

We modeled the CME using a cone model, a typical approximation commonly used to describe the properties of CMEs in the heliosphere (D. Odstrcil et al. 2004; J. Pomoell & S. Poedts 2018). In our model, the CME is initialized as a circular perturbation with time-dependent angular width and radius that evolve sinusoidally. Accordingly, we use

$$(\phi - \phi_{\text{CME}})^2 + (\theta - \theta_{\text{CME}})^2 < \alpha(t)^2, \tag{12}$$

$$\alpha(t) = \omega_{\text{CME}} \sin\left[\frac{\pi}{2} \frac{(t - t_{\text{onset}})}{t_{\text{half}}}\right],\tag{13}$$

$$t_{\text{half}} = R_{\text{in}} \frac{\tan(\omega_{\text{CME}}/2)}{v_{\text{CME}}},\tag{14}$$

where $\phi_{\rm CME}$ and $\theta_{\rm CME}$ are the CME center coordinates, $\alpha(t)$ the angular extent, $\omega_{\rm CME}$ the angular width, $t_{\rm onset}$ the onset time, $t_{\rm half}$ the insertion half-time, $R_{\rm in}=0.14$ au, the location of the inner boundary, and $v_{\rm CME}$ the CME speed.

To simulate the 2012 July 23 CME event in sunRunner3D, we extracted event parameters from the DONKI database⁹ and LASCO coronagraph data. CME speed at 31 R_{\odot} was obtained from a second-order fit in the SOHO LASCO CME Catalog. The values of $\phi_{\rm CME}$ and $\theta_{\rm CME}$ in the heliocentric Earth equatorial coordinates were converted to the Carrington coordinates using SunPy to match our

⁹ https://kauai.ccmc.gsfc.nasa.gov/DONKI/
10 https://cdaw.gsfc.nasa.gov/CME_list/

simulation framework. Further information on this simulation is presented in Appendices A and B.

In summary, the input parameters used for this event are as follows: detection time = 2012 July 23 T02: 36:00, $t_{\rm onset}$ = 240 h, $t_{\rm half}$ = 120 h, $\theta_{\rm CME}$ = 75.0, $\phi_{\rm CME}$ = 87.2, $\omega_{\rm CME}$ = 88.0, and $v_{\rm CME}$ = 2000 km s⁻¹.

2.4. Synthetic White Light

To compute simulated brightness and polarized brightness images from the simulation results, we use a forward modeling technique based on the Thomson scattering formulation originally described by D. E. Billings (1966). In particular, sunRunner3D provides full 3D electron density distributions, which we integrate along lines of sight to synthesize the observed white-light emission. The total brightness is calculated by summing the scattered intensity from all electrons along the line of sight, taking into account the geometry-dependent scattering efficiency. Polarized brightness is derived by computing the component of scattered light polarized perpendicular to the scattering plane, which emphasizes density structures nearer the plane of the sky. We implement these calculations using a tool, getpb, which projects the model results into the observer's geometry, including spacecraft or ground-based eclipse locations, and applies the appropriate scattering physics. This approach enables the generation of synthetic data for direct comparison with coronagraph, heliospheric, or eclipse observations, closely resembling those expected from the upcoming Polarimeter to UNify the Corona and Heliosphere (PUNCH) mission (D. Kolinski et al. 2022). The method builds on the foundations of D. E. Billings (1966), with refinements from modern treatments that extended the Thomson scattering theory and addressed practical considerations for heliospheric imaging (T. A. Howard & C. E. DeForest 2012).

3. Results

3.1. Oscillatory Modes Driven by CME

The CME is launched 240 hr after the simulation starts, following a \sim 230 hr relaxation period for the solar wind. Thus, the CME is injected approximately 10 hr after the solar wind reaches a steady state. The top-left panel of Figure 2 shows a 3D snapshot at t=252 hr, with volume-rendered number density (saturated at 500 cm⁻³) highlighting the CME structure. The blue line denotes the propagation direction of the CME.

To assess CME-driven dynamics, we apply vectorial SPOD to MHD variables as described in Equation (4), ensuring that intervariable correlations are preserved by ranking modes according to kinetic energy content. As SPOD generates as many modes as time frames, we consider the first 10 modes, which account for the most significant perturbations. Among these, we select the modes that exhibit oscillatory behavior in their time coefficients, indicating periodic structures such as propagating waves. Mode pairs were then identified based on the similarity of their spatial structures and the correlation of their temporal coefficients. This selection procedure has been applied consistently to all SPOD analyses presented in the Letter. The SPOD analysis spans from t = 180 to 398 hr. The other panels in Figure 2 show time-distance diagrams along the blue line reconstructed using pairs of SPOD modes to reconstruct perturbation propagation. The top row shows

time-distance diagrams of $\log_{10}(p)$, $\log_{10}(N_p)$, and $\log_{10}(T_p)$; the middle row displays perturbations in the velocity components v_x , v_y , and v_z ; and the bottom row presents perturbations in the magnetic field components. The magnitudes of all physical variables were min-max normalized. From each reconstructed 2D time-distance diagram, we normalized the data and identified the wave front as the first prominent peak in the radial profile at each time step using a peak detection algorithm. A straight line was then fitted to the points along the wave front using a least-squares regression, with the slope giving the propagation speed. Fits were only retained when at least five valid points were available and the coefficient of determination satisfied $R^2 > 0.9$. This procedure was applied consistently to both the observational and simulation data. For modes 1 and 2, a strong, fast perturbation emerges in all variables, propagating at speeds exceeding 1000 km s⁻¹ and persisting for approximately 60 hr before dissipating. This is likely the signature of the CME initiating and propagating through the domain. The bottom panels show reconstructions of modes 3-4 and 5-6. Unlike the leading modes, the higher-order modes' time-distances reveal signatures consistent with two fast magnetoacoustic waves with initial speeds near 1000 km s⁻¹. Both waves decelerate significantly after about 24 hr, dropping below 500 km s⁻¹, which suggests that the propagation speed decreases with radial distance as the wave energy spreads over an increasingly large area.

Similar wave signatures emerge when SPOD is applied to time series of synthetic white light, as indicated by perturbation reconstructions using modes 5-6 and 7-8 (Figure 3), reinforcing the notion that fast magnetoacoustic waves observed in simulations should also be detectable in coronagraph data. The time-distance diagrams in Figure 3 were computed along the blue line indicated in Figure 2. To quantify the dominant periodicities, we applied a fast Fourier transform (FFT) to the reconstructed time series of intensity fluctuations extracted from the time-distance plots at a heliocentric distance of 0.5 au, corresponding to the midpoint of the simulation domain. The FFT was preferred over a wavelet analysis to obtain a direct estimate of the dominant frequency from the limited-duration, quasiperiodic signal. The time series were detrended and zero-padded by a factor of 4 to improve frequency resolution. The statistical significance of the spectral peaks was assessed using a Monte Carlo permutation test following S. Jafarzadeh et al. (2025). Five hundred surrogate time series were generated using the iterative amplitude adjusted Fourier transform method, which preserves both the amplitude distribution and the power spectrum of the original signal. All analyzed signals exhibit FFT peaks exceeding the 99% confidence level, indicating statistically significant periodicities, and suggesting the presence of long-lived compressible structures in the inner heliosphere. The dominant periods are 176, 97.8, 67.7, and 58.7 hr for mode pairs 1–2, 3–4, 5–6, and 7–8, respectively.

3.2. Wave Detection in LASCO C3

We applied SPOD to LASCO C3 white-light intensity perturbations to examine the CME evolution in observational data. Figure 4 displays a LASCO C3 image taken shortly after the CME onset (top left), along with the reconstructed perturbations using modes 4 and 5 (top middle) and modes 7 and 8 (top right). Three radial lines (labeled 1–3) are overlaid

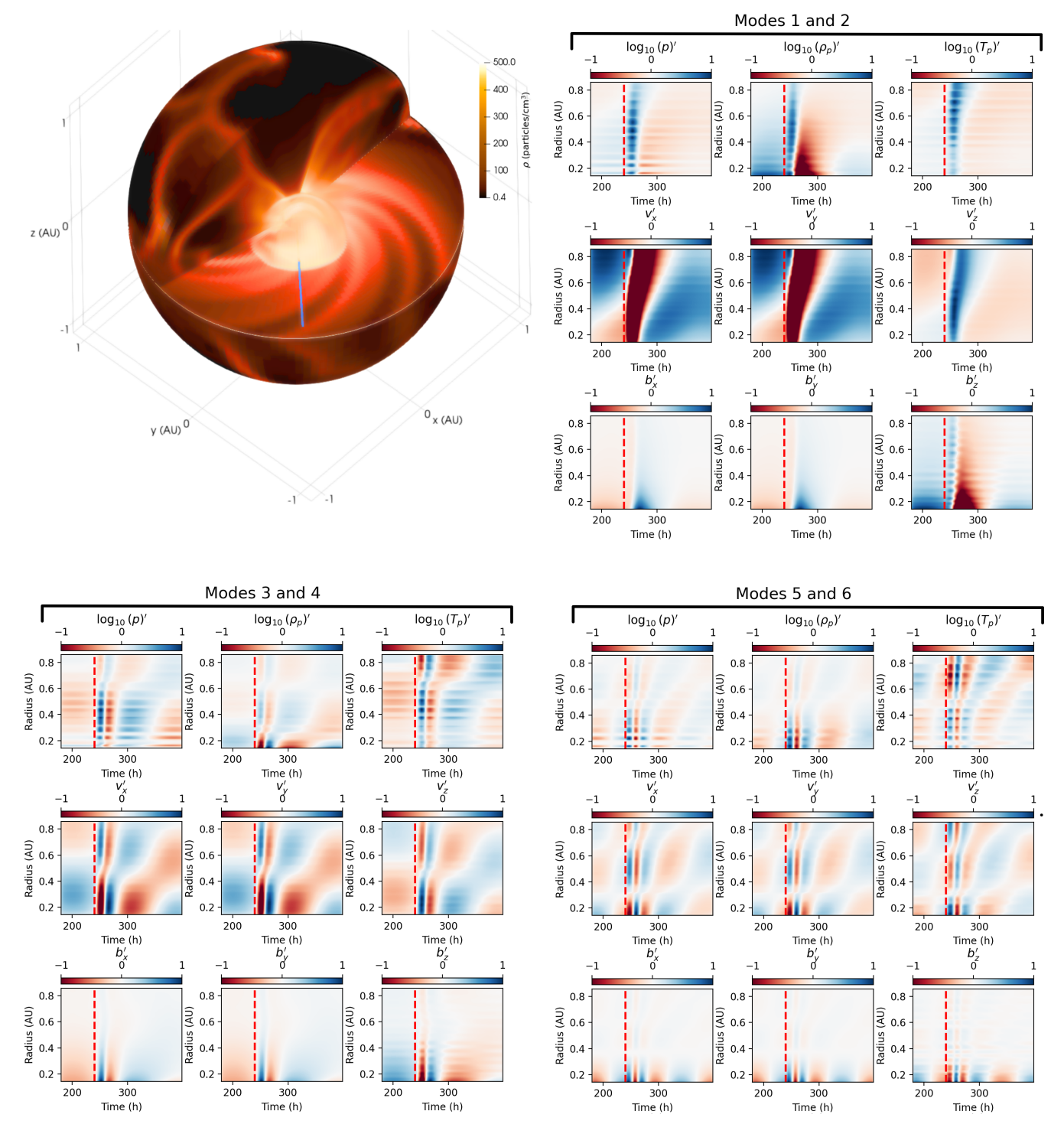


Figure 2. Top-left panel: 3D view of the simulation domain, 12 hr after CME onset. This panel shows the proton number density, volume-rendered and saturated at 500 particles cm⁻³, highlighting the propagating CME structure. The blue line indicates the direction of CME propagation. Top-right and bottom panels: time-distance diagrams of the perturbation reconstructions for the variables $\log_{10}(p)$, $\log_{10}(N_p)$, $\log_{10}(N_p)$, $\log_{10}(V_p)$, v_x , v_y , and v_z , using modes 1–2, 3–4, and 5–6. The symbol 'denotes perturbed variables, and the time-distance profiles were computed along the blue line shown in the top-left panel. The red dashed line marks the onset of the CME in the simulation.

to guide the extraction of intensity profiles. The bottom panels show time–distance diagrams along each line, with distance in solar radii (R_{\odot}) and time in hours. The CME begins at t=2 hr. The red and blue regions indicate SPOD-reconstructed positive and negative intensity perturbations, respectively, tracing CME-driven structures.

SPOD analysis of LASCO C3 perturbations reveals distinct propagation features by pairs of SPOD modes. For example, modes 4 and 5 show wave fronts traveling at 1200 km s⁻¹ and quickly fading away, while modes 7 and 8 display wave fronts decelerating from approximately 1200 to around 700 km s⁻¹ before vanishing. Following the same approach as before, we

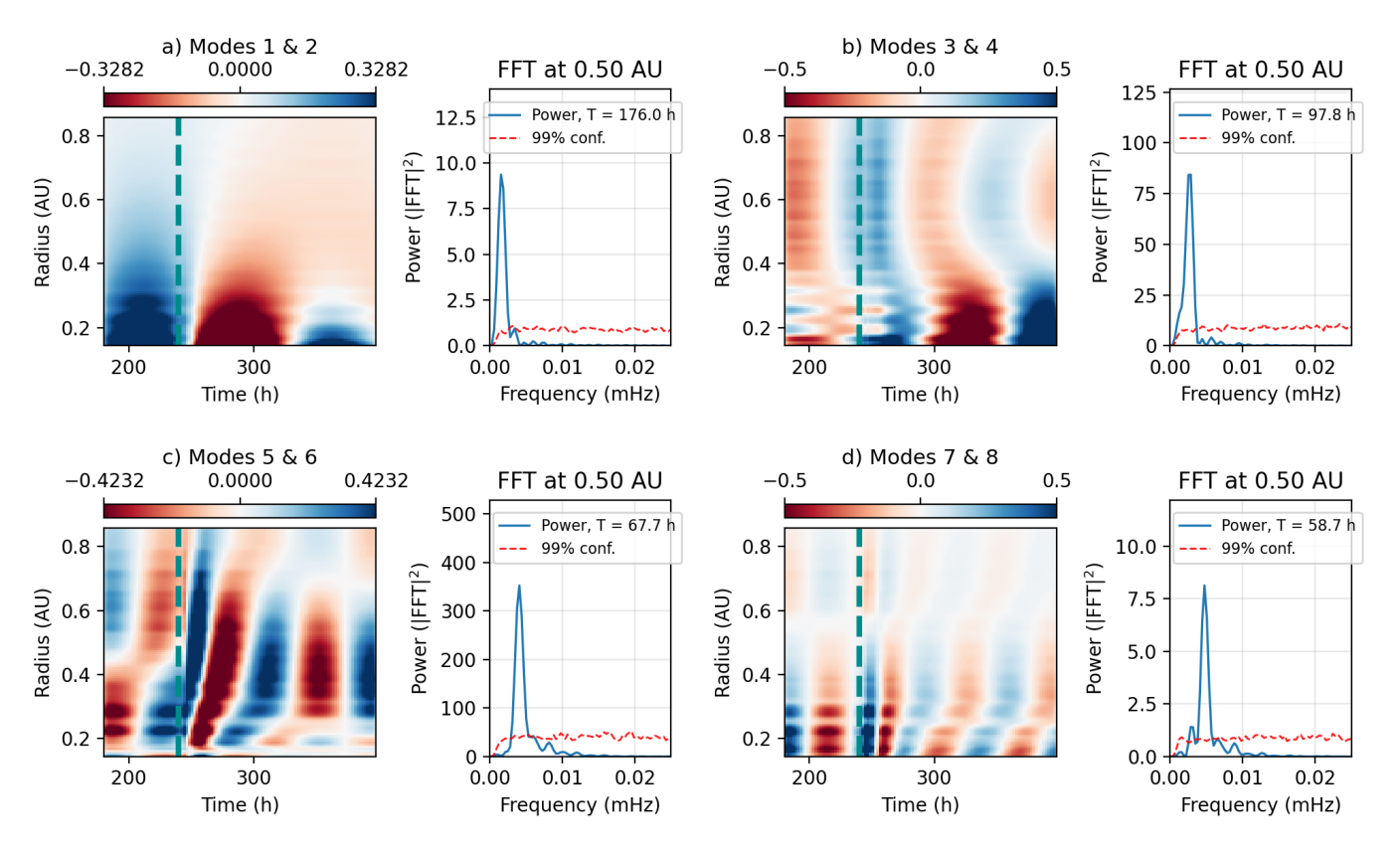


Figure 3. Time–distance diagrams along the blue line shown in Figure 2, reconstructed from the simulated white-light perturbations using modes (a) 1–2, (b) 3–4, (c) 5–6, and (d) 7–8. For each mode pair, the left panel shows the temporal evolution of the reconstructed perturbation as a function of heliocentric distance, while the right panel displays the corresponding FFT of the signal extracted at R = 0.50 au, with the dominant oscillation period (T) indicated in each plot. The onset of the CME is marked by the dashed dark-cyan line.

computed the FFT of the signal recovered from the timedistance plots, using the time series extracted at a heliocentric distance of 10 R_{\odot} , which corresponds to the middle of the distance range in the time-distance diagram. In this case, the confidence analysis was performed using surrogate time series of the signal along line 1, which lies along the CME propagation direction. The perturbations reconstructed from modes 4-5 exhibit a dominant frequency of 0.044 mHz (period \approx 6.4 hr) and persist for roughly one cycle, whereas modes 7–8 show a higher frequency of 0.096 mHz (period ≈ 2.9 hr) that remains coherent for over 5 hr. The LASCO images analyzed with SPOD are based on Thomson-scattered visible light, which is directly proportional to the line-of-sight integrated electron density. Therefore, any perturbation identified in our time-distance or SPOD analysis must reflect changes in plasma density. As such, the observed propagating features are inherently compressive. Noncompressive modes, such as purely Alfvénic waves, do not produce detectable signatures in white-light coronagraph data, since they do not induce density variations measurable via Thomson scattering.

Figure 5 displays the circular time-distance diagrams showing perturbations emerging at CME onset. The first panel shows the LASCO C3 image overplotted by the analyzed circular radius: $5.95R_{\odot}$ in red, $14.8R_{\odot}$ in blue, and $23.66R_{\odot}$ in green. Angles are also indicated. The second column shows the circular time-distance diagrams along those radii of the original LASCO C3 data for the analyzed time interval. The reconstructed perturbations obtained via POD and visualized

using circular time-distance diagrams are shown in the third and fourth columns. Modes 4 and 5 (third column in Figure 5) reconstruct a perturbation that exhibits a sharp increase in amplitude at different radii coinciding with the onset of the CME, consistent with impulsive and coherent energy release and the formation of a compressive front similar to a shock in the corona. Although this feature resembles a fast-mode shock, we note that in situ data from STEREO-A did not reveal a classical shock signature for this event (C. T. Russell et al. 2013). This suggests that the observed coronal front may represent a transient, possibly subfast mode, or mediated shock that dissipated or did not persist to 1 au. The subsequent decaying oscillations (Figure 5, third column) suggest compressional disturbances dissipating via geometrical spreading and energy losses in the expanding corona. The timing of the peak supports its association with a pressure discontinuity triggered by CME initiation. This behavior supports the presence of a CME-driven compressive wave front, consistent with a coronal shock that perturbs the corona and inner heliosphere. SPOD modes 7 and 8 (fourth column) reveal a second global circularly fast propagating compressive wave triggered across all radii at the onset of the CME, with oscillations lasting up to \sim 12 hr. The coexistence of a rapidly propagating compressive front and a long-lived global mode suggests a dual-wave coronal response to the CME, involving both localized shock-like disturbances and global fast-mode wave activity.

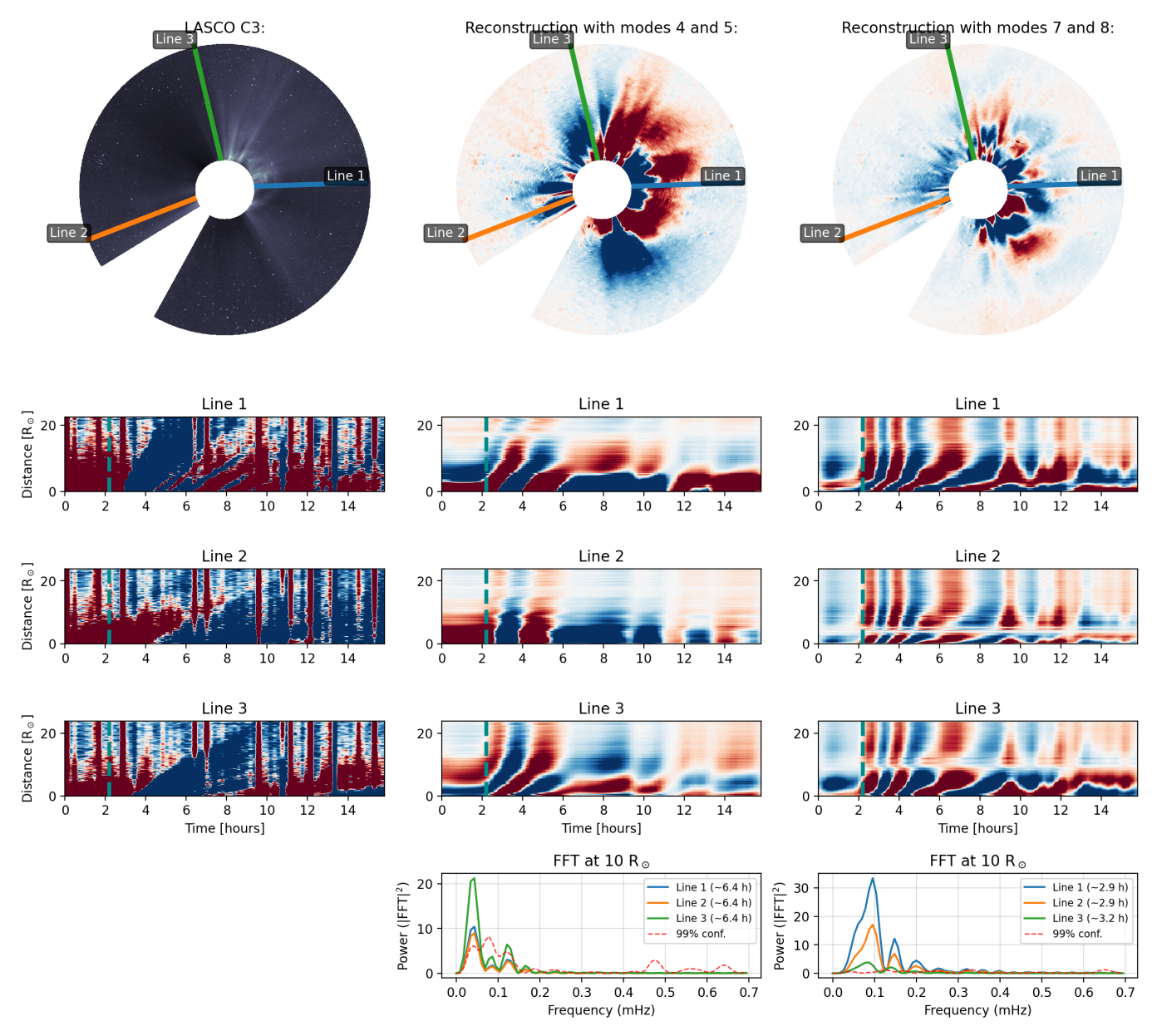


Figure 4. Analysis of LASCO C3 white-light perturbations using selected modes of SPOD. Top row: LASCO C3 image a few hours after the CME onset, showing the three analyzed radial directions (lines 1–3). Middle panels: time–distance maps along each line. The first column shows intensity perturbations, while the second and third columns show reconstructions of perturbations using SPOD modes 4–5 and 7–8, respectively. The CME onset is marked by a dashed dark-cyan line. Red and blue hues represent positive and negative fluctuations in the perturbations or SPOD intensity modes. Bottom row: FFT power spectra of the reconstructed intensity fluctuations at $10 R_{\odot}$. The dashed red line marks the 99% confidence level derived from a Monte Carlo permutation test; spectral peaks above this line are statistically significant.

4. Discussion and Conclusion

We presented the first combined observational and numerical evidence for a dual-wave response to a CME in the outer corona and inner heliosphere. We identified a rapidly propagating compressive front consistent with a fast-mode shock and a persistent global coronal oscillation. This dual behavior is evident in the SPOD-decomposed LASCO data and an MHD simulation, with each mode exhibiting distinct spatial and temporal evolution patterns. The compressive front extends approximately 60° to 90° around the CME nose, while the global mode spans nearly the full 360° angular extent of the C3 field of view. This result provides new support for the idea that CMEs distribute energy into multiple MHD wave components.

The global mode is consistent with previous interpretations of large-scale coronal oscillations and EUV waves (e.g., W. Liu et al. 2018; R. Zheng et al. 2019), while the compressive front aligns with piston- and bow-shock models (Y. D. Liu et al. 2017). The ability of the SPOD method to isolate these components confirms its value in disentangling overlapping wave structures in coronagraph data and demonstrates its consistency with controlled numerical experiments.

The CME-driven compressive front, observed for ~ 2.5 hr in LASCO data, shows propagation speeds exceeding 1000 km s⁻¹, similar to fast-mode EUV waves and white-light shock signatures (N. Gopalswamy et al. 2008; V. Ontiveros & A. Vourlidas 2009). In the simulation, this front persists for ~ 60 hr and reaches 1 au, though its morphology varies with distance. However, in situ

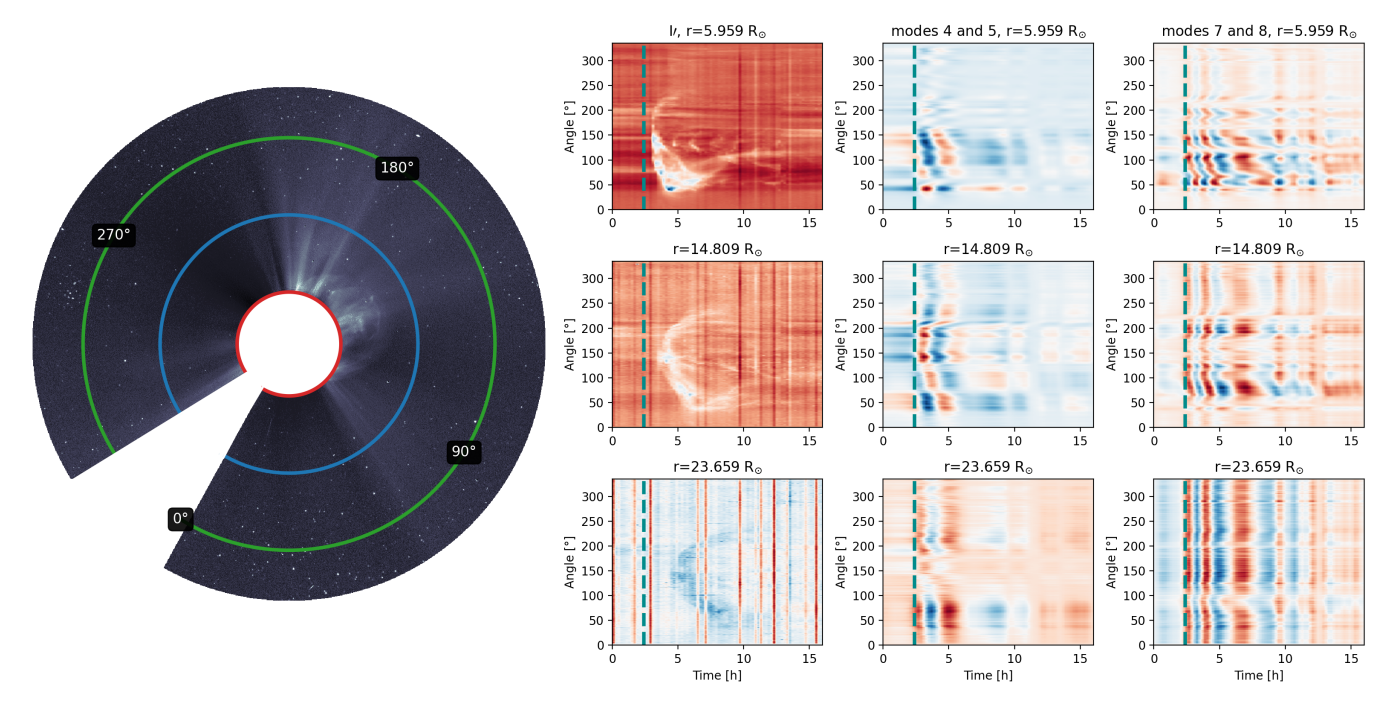


Figure 5. Analysis of LASCO C3 white image perturbations using selected modes of SPOD. The top panel shows a polar representation of the corona with concentric circles. The right panels display the corresponding time–distance diagrams for each circle, where the vertical axis represents the angle along the curve, and the horizontal axis indicates the time in hours. The CME onset is marked by the dark-cyan dashed line. Red and blue hues denote positive and negative fluctuations in the SPOD intensity modes.

observations from STEREO-A (C. T. Russell et al. 2013) show no clear fast-mode shock signature, suggesting that the shock-like disturbance we observe in the outer corona may have been suppressed or mediated by upstream conditions, consistent with scenarios of shock weakening or dissipation in the heliosphere (e.g., D. N. Baker et al. 2013; P. Riley et al. 2016).

The detection of global compressive oscillations in the outer corona has several important implications. This case indicates that strong CMEs may generate large-scale, coherent disturbances that extend beyond the eruption site, suggesting that CME-driven perturbations can influence the global structure of the outer corona and inner heliosphere. The results further imply that global, CME-driven coronal oscillations could be analogous to—and possibly represent a high-altitude extension of—EUV waves reported in previous studies (e.g., H. Hu et al. (2024) and as seen in the nearly spherical shocks reported by Y. D. Liu et al. (2017) for the same event). This approach also helps constrain how compressive energy dissipates with distance, providing insight into damping and geometric expansion effects in the outer corona. If similar oscillations are confirmed in other CME events, they could serve as a new diagnostic of the global coronal response to eruptive activity, with implications for space-weather modeling and for understanding the evolution of coronal disturbances into interplanetary shocks. The analysis of synthetic white-light data from simulations further suggests that such wave signatures should be detectable with future missions such as PUNCH. Continued studies of additional events with comparable temporal and spatial coverage will be essential to assess how common these global oscillations are and to clarify their role in the large-scale dynamics of the solar corona.

Acknowledgments

S.S.A.S., V.F., G.V., and I.B. are grateful to The Royal Society, International Exchanges Scheme, collaboration with

Greece (IES/R1/221095) and India (IES/R1/211123). S.S.A.S., V.F., and G.V. are grateful for the Science and Technology Facilities Council (STFC) grants ST/V000977/1, ST/Y001532/1. L.A.C.A.S. acknowledges STFC for support from grant No. ST/X001008/1. L.F.G.B. was supported by Brazilian agency CAPES under grant (88887.006144/2024-00 - 2200101-8 UFC). E.L.R. acknowledges support by Brazilian agency CNPq under grant 306920/2020-4. S.S.A.S., V.F., and E.L.R. would like to thank the International Space Science Institute (ISSI) in Bern, Switzerland, for the hospitality provided to the team on "Opening New Avenues in Identifying Coherent Structures and Transport Barriers in the Magnetized Solar Plasma." V.F. also acknowledges ISSI's support for the teams on "The Nature and Physics of Vortex Flows in Solar Plasmas" and "Tracking Plasma Flows in the Sun's Photosphere and Chromosphere: A Review & Community Guide." J.J.G.A. acknowledges the support of the Secretaría de Ciencia, Humanidades, Tecnología e Innovación (SECIHTI) under grant 319216, Modalidad: Paradigmas y Controversias de la Ciencia 2022, and UNAM-PAPIIT project IA100725. P.R. and M.B.N. acknowledge support from NSF's PREEVENTS program (grant No. ICER-1854790), NASA's LWS Strategic Capabilities (80NSSC22K0893), and the PSP WISPR contract NNG11EK11I to NRL (under subcontract N00173-19-C-2003 to PSI).

Appendix A Boundary Conditions

To generate the boundary conditions used by PLUTO, we employed the CORona–HELiosphere (CORHEL) modeling suite (J. A. Linker et al. 2009), which models the ambient solar corona and inner heliosphere for specific periods of interest, labeled in terms of Carrington rotations (CRs). The primary input to CORHEL consists of synoptic maps of the radial photospheric magnetic field, B_r , provided by observatories

such as the National Solar Observatory, the Synoptic Optical Long-term Investigations of the Sun, the Global Oscillation Network Group, and the Helioseismic and Magnetic Imager on board the Solar Dynamics Observatory. A key feature of CORHEL's modeling strategy is the separation of the coronal and heliospheric domains, using different codes and physical approximations in each region. In particular, the outer boundary of the coronal solution is placed beyond both the Alfvén and sound speed critical points (typically at 20–30 solar radii, R_{\odot}). This coronal solution is then used to drive the heliospheric model (which extends up to 230 R_{\odot}), and can be calculated either in an inertial frame or in a corotating frame with the Sun.

Using the synoptic maps, the coronal model is executed with the magnetohydrodynamic algorithm outside a Sphere (MAS) code (Z. Mikić & J. A. Linker 1996; Z. Mikić et al. 2018; P. Riley et al. 2021) until a relaxed state is obtained, which in turn provides the boundary conditions for the heliospheric simulations. CORHEL solutions are available on request through the Community Coordinated Modeling Center. In this work, we take advantage of the fact that the boundary conditions required to represent the background solar wind for CR 2126 are directly available at https://www.predsci.com/data/runs/. These files are already formatted for use with the

PLUTO code and include all relevant physical variables (e.g., number density, radial velocity, radial magnetic field, and temperature). We use these data to specify the inner boundary at $R_b=0.14$ au, and as the initial condition throughout the computational domain.

Appendix B Shocks and Plasma Structures in the CME Simulation

Figure 6 shows the simulation results 20 hr after the CME launch in the equatorial plane. Panel (a) displays the radial velocity V_r (km s⁻¹), where the red arrow marks the sharp velocity jump associated with the forward shock. Panel (b) shows the logarithm of the proton density N_p (cm⁻³); the red arrow indicates the compression region ahead of the ejecta, and the black arrow marks the trailing reverse shock, both appearing as localized density enhancements. Panel (c) presents the logarithm of the proton temperature T_p (K), where the yellow arrow highlights the strong temperature gradient produced by shock heating at the forward front. Panel (d) depicts the radial magnetic field B_r (nT); the black arrows denote magnetic distortions of the Parker spiral, where the CME alters the orientation and polarity of the background solar wind magnetic field.

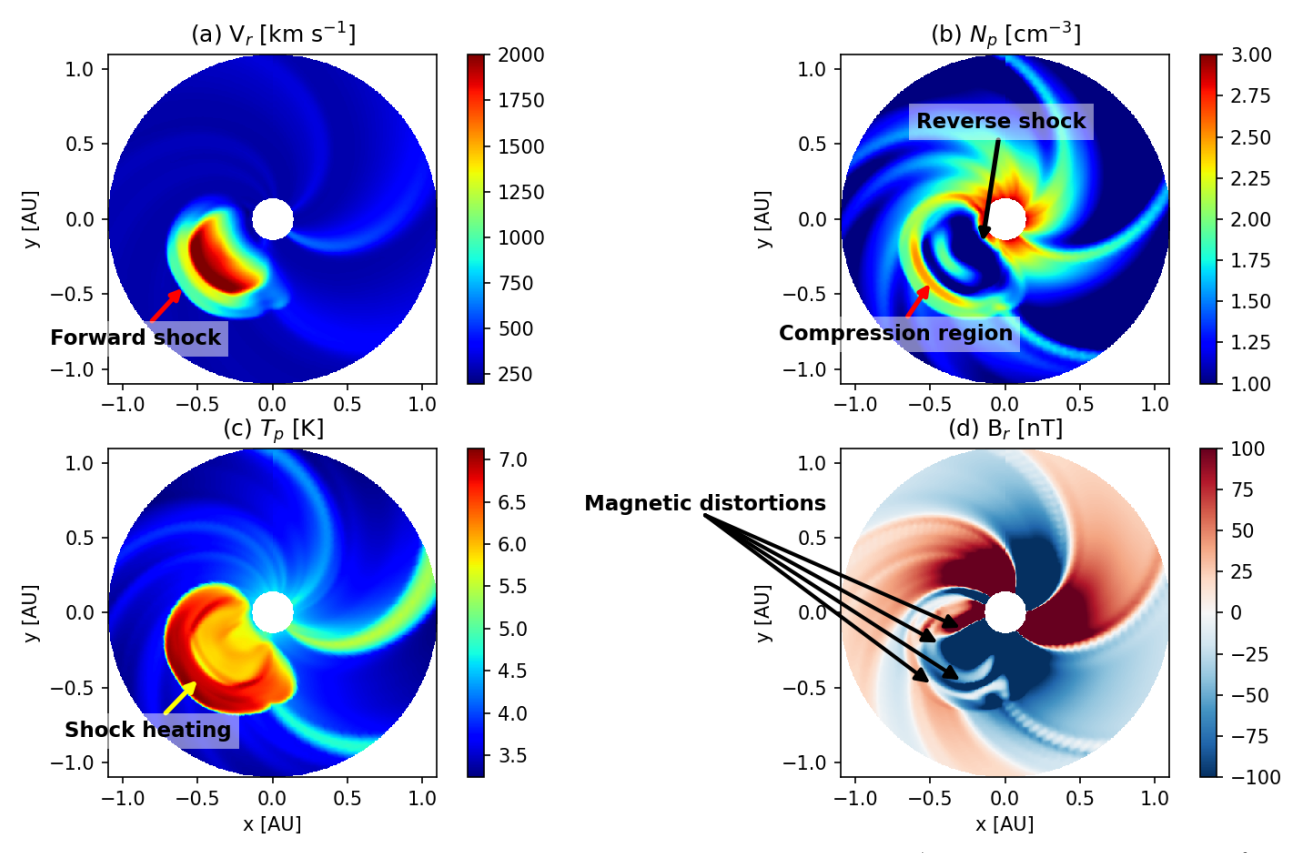


Figure 6. Equatorial slice of the CME simulation 20 hr after launch. Panels show (a) radial velocity V_r (km s⁻¹), (b) log of proton density N_p (cm⁻³), (c) log of proton temperature T_p (K), and (d) radial magnetic field B_r (nT). Red, black, and yellow arrows indicate, respectively, the forward shock and compression region, the reverse shock and magnetic distortions of the Parker spiral, and the shock heating at the forward front.

9

¹¹ https://ccmc.gsfc.nasa.gov

ORCID iDs

```
Suzana S. A. Silva https://orcid.org/0000-0001-5414-0197 J. J. González-Avilés https://orcid.org/0000-0003-0150-9418

Pete Riley https://orcid.org/0000-0002-1859-456X
```

Pete Riley https://orcid.org/0000-0002-1859-456X
Michal Ben-Nun https://orcid.org/0000-0002-9164-0008
Erico L. Rempel https://orcid.org/0000-0002-4971-5854
Leonardo F. G. Batista https://orcid.org/0000-0002-2938-180X

Gary Verth https://orcid.org/0000-0002-9546-2368
Istvan Ballai https://orcid.org/0000-0002-3066-7653
Chia-Hsien Lin https://orcid.org/0000-0002-5230-0270
Luiz A. C. A. Schiavo https://orcid.org/0000-0002-5082-1398

Viktor Fedun https://orcid.org/0000-0002-0893-7346

References

```
Aguilar-Rodriguez, E., González-Avilés, J. J., Riley, P., et al. 2024, MNRAS,
   529, 1250
Baker, D. N., Li, X., Pulkkinen, A., et al. 2013, SpWea, 11, 585
Ballai, I., Erdélyi, R., & Pintér, B. 2005, ApJL, 633, L145
Biesecker, D. A., Myers, D. C., Thompson, B. J., Hammer, D. M., &
   Vourlidas, A. 2002, ApJ, 569, 1009
Billings, D. E. 1966, A Guide to the Solar Corona (Academic)
Chen, P. F., Ding, M. D., & Fang, C. 2005, SSRv, 121, 201
Chen, Y. 2013, ChSBu, 58, 1599
De León-Alanis, L., González-Avilés, J. J., Riley, P., & Ben-Nun, M. 2024,
   RMxF, 70, 031501
González-Avilés, J. J., Riley, P., Ben-Nun, M., Mayank, P., & Vaidya, B.
   2024, JSWSC, 14, 12
Gopalswamy, N., Xie, H., Akiyama, S., Mäkelä, P. A., & Yashiro, S. 2014,
       &S, 66, 104
Gopalswamy, N., Yashiro, S., Michalek, G., et al. 2008, EM&P, 104, 295
Gopalswamy, N., Yashiro, S., Thakur, N., et al. 2016, ApJ, 833, 216
```

```
Harten, A., Lax, P. D., & van Leer, B. 1997, in Upwind and High-Resolution
  Schemes, ed. M. Y. Hussaini, B. van Leer, & J. Van Rosendale
  (Springer), 53
Howard, T. A., & DeForest, C. E. 2012, ApJ, 752, 130
Hu, H., Zhu, B., Liu, Y. D., et al. 2024, ApJ, 976, 9
Huang, T., Yang, G., & Tang, G. 1979, ITASS, 27, 13
Jafarzadeh, S., Jess, D. B., Stangalini, M., et al. 2025, NRvMP, 5, 21
Kolinski, D., Deforest, C., Gibson, S., et al. 2022, TESS, 54, 2022n7i125p22
Kwon, R.-Y., Ofman, L., Olmedo, O., et al. 2013, ApJ, 766, 55
Kwon, R.-Y., Zhang, J., & Olmedo, O. 2014, ApJ, 794, 148
Linker, J. A., Riley, P., Mikic, Z., et al. 2009, in AGU Fall Meeting, SA43A-
  1612 (AGU)
Liu, W., Jin, M., Downs, C., et al. 2018, ApJL, 864, L24
Liu, Y. D., Hu, H., Zhu, B., Luhmann, J. G., & Vourlidas, A. 2017, ApJ, 834, 158
Mayank, P., Vaidya, B., & Chakrabarty, D. 2022, ApJS, 262, 23
Mignone, A., Bodo, G., Massaglia, S., et al. 2007, ApJS, 170, 228
Mikić, Z., Downs, C., Linker, J. A., et al. 2018, NatAs, 2, 913
Mikić, Z., & Linker, J. A. 1996, AIPC, 382, 104
Odstrcil, D., Riley, P., & Zhao, X. P. 2004, JGRA, 109, A02116
Ontiveros, V., & Vourlidas, A. 2009, ApJ, 693, 267
Pomoell, J., & Poedts, S. 2018, JSWSC, 8, A35
Powell, K. G. 1997, in Upwind and High-Resolution Schemes, ed.
  M.Y. Hussaini, B. van Leer, & J. Van Rosendale (Springer), 570
Riley, P., & Ben-Nun, M. 2022, Univ, 8, 447
Riley, P., Ben-Nun, M., González-Avilés, J., et al. 2025, JSWSC, 15, 17
Riley, P., Caplan, R. M., Giacalone, J., Lario, D., & Liu, Y. 2016, ApJ, 819, 57
Riley, P., Lionello, R., Caplan, R. M., et al. 2021, A&A, 650, A19
Russell, C. T., Mewaldt, R. A., Luhmann, J. G., et al. 2013, ApJ, 770, 38
Savitzky, A., & Golay, M. J. E. 1964, AnaCh, 36, 1627
Sieber, M., Paschereit, C. O., & Oberleithner, K. 2016, JFM, 792, 798
Thompson, B. J., & Myers, D. C. 2009, ApJS, 183, 225
Veronig, A. M., Muhr, N., Kienreich, I. W., Temmer, M., & Vršnak, B. 2010,
    pJL, 716, L57
Vršnak, B., & Cliver, E. W. 2008, SoPh, 253, 215
Wang, H., Shen, C., & Lin, J. 2009, ApJ, 700, 1716
Warmuth, A. 2011, PPCF, 53, 124023
Wills-Davey, M., DeForest, C., & Stenflo, J. O. 2007, ApJ, 664, 556
Zhang, B., Sorathia, K. A., Lyon, J. G., Merkin, V. G., & Wiltberger, M. 2019,
   JCoPh, 376, 276
Zheng, R., Xue, Z., Chen, Y., Wang, B., & Song, H. 2019, ApJ, 871, 232
```